

Cosmological nonlinear structure formation in full general relativity

José M. Torres,¹ Miguel Alcubierre,¹ Alberto Diez-Tejedor,² and Darío Núñez¹

¹*Instituto de Ciencias Nucleares, Universidad Nacional Autónoma de México,
Circuito Exterior C.U., A.P. 70-543, México D.F. 04510, México*

²*Santa Cruz Institute for Particle Physics and Department of Physics,
University of California, Santa Cruz, CA, 95064, USA*

(Dated: August 8, 2018)

We perform numerical evolutions of cosmological scenarios using a standard general relativistic code in spherical symmetry. We concentrate on two different situations: initial matter distributions that are homogeneous and isotropic, and perturbations to those that respect the spherical symmetry. As matter models we consider the case of a pressureless perfect fluid, *i.e.* dust, and the case of a real massive scalar field oscillating around the minimum of the potential. Both types of matter have been considered as possible dark matter candidates in the cosmology literature, dust being closely related to the standard cold dark matter paradigm. We confirm that in the linear regime the perturbations associated with these types of matter grow in essentially the same way, the main difference being that in the case of a scalar field the dynamics introduce a cutoff in the power spectrum of the density perturbations at scales comparable with the Compton wavelength of the field. We also follow the evolutions well beyond the linear regime showing that both models are able to form structure. In particular we find that, once in the nonlinear regime, perturbations collapse faster in a universe dominated by dust. This is expected to delay the formation of the first structures in the scalar field dark matter scenario with respect to the standard cold dark matter one.

PACS numbers: 95.30.Sf, 95.35.+d, 98.80.Jk

I. INTRODUCTION

Structure formation as a consequence of the dynamical instability of self-gravitating matter constitutes a cornerstone of modern physical cosmology. As long as the deviations with respect to a homogeneous and isotropic universe are small, it is always possible to develop a self-consistent linear order theory where approximate analytic solutions can be found [1–3]. However, when the inhomogeneities grow and reach the nonlinear regime those solutions fail and numerical techniques become necessary.

For the case of a universe dominated by classical particles the evolution of the cosmological perturbations under the influence of (Newtonian) gravity can be followed using N-body simulations (see *e.g.* [4] and references therein). However, when a description in terms of particles is not viable, we need other techniques in order to address nonlinear structure formation. That is the case, for instance, for models that consider dark matter and/or dark energy as coherent macroscopic excitations of a boson field (*e.g.* nonthermal axionlike candidates for dark matter [5–9], quintessence models of dark energy [10, 11], *k*-essence [12]), or models that propose a modification of general relativity (*e.g.* MOND [13, 14], Einstein-aether [15, 16], massive gravity [17, 18]), just to name some examples.

In this paper we adapt a numerical relativity code in spherical symmetry to evolve cosmological scenarios and deal with the problem of nonlinear structure formation in situations where a description of matter in terms of fields is necessary. We use the OllinSphere2 code described in Ref. [19], which solves the full Einstein field equations in spherical symmetry coupled to different types of matter.

The code uses the standard 3+1 formulation of general relativity with a strongly hyperbolic, well-posed system of evolution equations [20]. Furthermore, it is regular in the sense that the variables behave smoothly at the origin [19, 21]. The OllinSphere2 code has been used previously to address problems involving spherically symmetric, self-gravitating compact objects in general relativity [22–24].

In this paper we use our code for the first time to study the cosmological evolution of inhomogeneous distributions of matter, also in spherical symmetry. Particular attention is given to the cases of a perfect fluid with no pressure (dust) and a massive scalar field oscillating around the minimum of the potential showing that, in the context of an expanding universe, small perturbations in both cases can develop structures around otherwise homogeneous and isotropic initial data. This is indeed an interesting result: it has been previously argued that, since the small perturbations of a canonical scalar field propagate at the speed of light [25, 26], the coherent macroscopic excitations of a boson field cannot give rise to a successful cosmological structure formation. This work, along with [27], aims to provide evidence supporting the idea that a free classical massive scalar field in a cosmological context can lead to large scale structure formation.

This paper is organized as follows. In Section II we review the 3+1 formulation of general relativity. We also present the Baumgarte-Shapiro-Shibata-Nakamura (BSSN) system of evolution equations implemented in the numerical code for the particular case of spherical symmetry [19, 28–30]. Next, in Section III we consider spatially flat, homogeneous and isotropic distributions of

matter. In Section IV we study the evolution of spherically symmetric distributions of matter that represent small perturbations away from homogeneity. The results of our numerical simulations are presented in Sections V and VI, where we consider cosmologies dominated by a pressureless perfect fluid, and by the coherent oscillations of a real massive scalar field, respectively. We find that the evolution of the linear order perturbations in a universe dominated by a scalar field is initially very similar to the case of a universe dominated by dust, but with a cutoff in the power spectrum at the Compton wavelength of the scalar particle (as was already known from previous analytical results, *e.g.* [31–35]). Once in the nonlinear regime, however, the evolution of the inhomogeneities for both types of matter differs: while the perturbations in the case of dust collapse very quickly, the growth of the perturbations in the case of a scalar field is more gradual, delaying the formation of the first structures in the universe.

We should mention at this point that during the final stage of preparation of this paper we became aware of two recent studies that address similar topics. On the one hand, the authors of [36] (see also Ref. [37]) consider the problem of structure formation in a universe dominated by an ultralight scalar field using a hydrodynamic code in full 3D, but they assume from the beginning a nonrelativistic, weak field approximation (see *e.g.* Refs. [38–41] for possible relativistic effects even in N-body simulations, and Ref. [42] for particular attention to the case of a scalar field). On the other hand in Ref. [43] the authors present a fully relativistic numerical code for the study of cosmological problems in spherical symmetry and use it to reproduce the analytical Lemaitre-Tolman-Bondi solution. We believe the results presented in this paper complement those previous studies. See also Refs. [44, 45] for other interesting recent applications of numerical relativity to cosmology, now in the context of the early universe.

II. SPACETIME DYNAMICS AS AN INITIAL VALUE PROBLEM

In order to analyze the nonlinear behavior of the perturbations of a Friedmann universe we find it convenient to formulate the evolution of the cosmological spacetime as an initial value problem. A usual way of doing that is to use the standard 3+1 formulation due to Arnowitt, Dessler and Misner (ADM) [46, 47], in which the spacetime is foliated into spatial hypersurfaces of constant time, and the spacetime line-element is given by (throughout the paper we use a signature $(-, +, +, +)$, and work in units such that $c = G = 1$):

$$ds^2 = (-\alpha^2 + \beta_i \beta^i) dt^2 + 2\beta_i dt dx^i + \gamma_{ij} dx^i dx^j. \quad (1)$$

Here α is a lapse function, β^i the shift vector, and γ_{ij} the metric tensor of the three-dimensional spatial hypersur-

faces. In general all of them are functions of the space-time coordinates (t, x^i) . Spatial indexes are raised and lowered with the spatial metric, *e.g.* $\beta_i = \gamma_{ij} \beta^j$, with $\gamma^{ij} \gamma_{jk} \equiv \delta_k^i$.

In the 3+1 formalism the basic dynamical quantities are the metric of the spatial hypersurfaces γ_{ij} , and the extrinsic curvature tensor of those hypersurfaces K_{ij} (see *e.g.* Eq. (4a) below for the definition of this tensor). There are also four gauge functions, the lapse α and the shift vector β^i , which are associated with the freedom in the choice of the coordinate system. In terms of these variables the Einstein field equations take the form of a constrained evolution system similar to Maxwell's in the case of electromagnetism.

The constraints are obtained when projecting the Einstein field equations along the normal direction to the spatial hypersurfaces. The resulting expressions contain no time derivatives and are called the Hamiltonian and momentum constraints:

$$\mathcal{H} := R + K^2 - K_{ij} K^{ij} - 16\pi\rho = 0, \quad (2a)$$

$$M^i := \nabla_j (K^{ij} - \gamma^{ij} K) - 8\pi j^i = 0. \quad (2b)$$

In the above equations $R := \gamma^{ij} R_{ij}$ is the trace of the Ricci tensor, $K := \gamma^{ij} K_{ij}$ is the trace of the extrinsic curvature, and ∇_i is the covariant derivative, all of them defined with respect to the spatial metric γ_{ij} . As usual ρ and j^i are the energy and momentum densities of matter as measured by observers that move along the normal trajectories to the spatial hypersurfaces, the so-called ‘‘Eulerian observers’’,

$$\rho := n^\mu n^\nu T_{\mu\nu}, \quad (3a)$$

$$j^i := -P^{i\mu} n^\nu T_{\mu\nu}. \quad (3b)$$

The above quantities are defined in terms of the stress-energy tensor of the matter fields, $T_{\mu\nu}$, with $n^\mu = (1/\alpha, -\beta^i/\alpha)$ the unit normal vector to the spatial hypersurfaces of constant time, and $P_\mu^\nu := \delta_\mu^\nu + n_\mu n^\nu$ the projection operator.

The dynamics of the gravitational field is obtained when one projects the Einstein equations onto the spatial hypersurfaces. Together with the definition of the extrinsic curvature, the evolution equations are given by

$$\partial_t \gamma_{ij} - \mathcal{L}_{\vec{\beta}} \gamma_{ij} = -2\alpha K_{ij}, \quad (4a)$$

$$\begin{aligned} \partial_t K_{ij} - \mathcal{L}_{\vec{\beta}} K_{ij} &= -\nabla_i \nabla_j \alpha \\ &+ \alpha (R_{ij} + K K_{ij} - 2K_{ik} K_j^k) \\ &+ 4\pi\alpha [\gamma_{ij} (S - \rho) - 2S_{ij}]. \end{aligned} \quad (4b)$$

Here $\mathcal{L}_{\vec{\beta}}$ is the Lie derivative along the direction of the shift vector, and S_{ij} the stress tensor measured by the Eulerian observers,

$$S_{ij} := P_i^\alpha P_j^\beta T_{\alpha\beta}, \quad (5)$$

with $S := \gamma^{ij} S_{ij}$ its trace. Equations (4) must be completed with the evolution equations for the matter fields

and gauge functions, as well as an appropriate set of initial data compatible with the constraints (2) and boundary conditions (see below for details).

Although in principle one can solve the above system of equations and obtain the future evolution of the space-time, it turns out that the mathematical properties of the system make it numerically unstable in practice. A great amount of work in the field of numerical relativity was focused on reformulating the system of evolution equations, by introducing auxiliary fields and/or modifying the evolution equations by adding terms proportional to the constraints, in order to render the system stable. Here we will employ the BSSN formulation [28, 29] adapted to curvilinear coordinate systems [19, 30], that results in a well-posed, strongly hyperbolic formulation of the 3+1 evolution equations. The BSSN formulation has proven to be very robust in practice and is widely used in numerical relativity.

Next we review the main ingredients of the BSSN formulation (with particular interest in the spherically symmetric case), and refer the reader to the literature on the subject [19, 20] for further details on its derivation. We begin by introducing a conformal decomposition of the spatial metric tensor of the form

$$\gamma_{ij} := e^{4\chi} \hat{\gamma}_{ij}, \quad \chi \equiv \ln \psi := \frac{1}{12} \ln(\gamma/\hat{\gamma}). \quad (6)$$

The conformal factor $e^{4\chi}$ introduced in Eq. (6) relates the physical volume element to the conformal one, which is assumed to take initially its flat-space value. In addition we have defined the determinant of the two spatial metric tensors, the physical $\gamma := \det(\gamma_{ij})$, and the conformal one, $\hat{\gamma} := \det(\hat{\gamma}_{ij})$.

We will also introduce the traceless conformal extrinsic curvature tensor,

$$\hat{A}_{ij} := e^{-4\chi} \left(K_{ij} - \frac{1}{3} \gamma_{ij} K \right), \quad (7)$$

and a combination of contracted Christoffel symbols, which we will call the ‘‘connection vector’’ from now on, of the form

$$\hat{\Delta}^i := \hat{\gamma}^{mn} (\hat{\Gamma}_{mn}^i - \hat{\Gamma}_{mn}^i). \quad (8)$$

The over-ring in Eq. (8) makes reference to some arbitrary background metric which, for simplicity, can be taken to be flat. Note that even though neither $\hat{\Gamma}_{mn}^i$ nor $\hat{\Gamma}_{mn}^i$ are true tensors, their difference is in fact a properly defined tensor, so that the quantity $\hat{\Delta}^i$ introduced above is a true vector. In the BSSN formulation the connection vector is considered to be an independent dynamical variable, and its definition is treated as an additional constraint.

For the case of spherical symmetry the equations above simplify considerably. In this case it is always possible to find a coordinate system where the metric tensor of the spatial hypersurfaces takes the form

$$\gamma_{ij} dx^i dx^j = e^{4\chi} (\hat{\gamma}_{\parallel} dr^2 + \hat{\gamma}_{\perp} r^2 d\Omega^2). \quad (9)$$

With this choice the connection vector has only the radial component different from zero, $\hat{\Delta}^i = (\hat{\Delta}^r, 0, 0)$. The traceless condition for the tensor \hat{A}_{ij} , together with the assumption of spherical symmetry, now guarantees that $\hat{A}_r^r = -2\hat{A}_\theta^\theta = -2\hat{A}_\varphi^\varphi := \hat{A}_{\parallel}$. Note that the dynamical quantities χ , $\hat{\gamma}_{\parallel}$, $\hat{\gamma}_{\perp}$, $\hat{\Delta}^r$, and \hat{A}_{\parallel} , as well as the trace of the extrinsic curvature K , are functions only of time and the radial coordinate r .

Although the numerical code does not impose any particular gauge, from now on and for the purposes of this paper it will be convenient to fix the shift vector to zero. In terms of the new variables the Hamiltonian and momentum constraints take the form

$$\mathcal{H} := R - \frac{3}{2} \hat{A}_{\parallel}^2 + \frac{2}{3} K^2 - 16\pi\rho = 0, \quad (10a)$$

$$M_r := \partial_r \hat{A}_{\parallel} - \frac{2}{3} \partial_r K + 6 \hat{A}_{\parallel} \partial_r \chi + \frac{3}{2} \hat{A}_{\parallel} \left(\frac{2}{r} + \frac{\partial_r \hat{\gamma}_{\perp}}{\hat{\gamma}_{\perp}} \right) - 8\pi j_r = 0, \quad (10b)$$

whereas for the evolution equations we find

$$\partial_t \chi = -\frac{1}{6} \alpha K, \quad (11a)$$

$$\partial_t \hat{\gamma}_{\parallel} = -2\alpha \hat{\gamma}_{\parallel} \hat{A}_{\parallel}, \quad (11b)$$

$$\partial_t \hat{\gamma}_{\perp} = \alpha \hat{\gamma}_{\perp} \hat{A}_{\parallel}, \quad (11c)$$

$$\begin{aligned} \partial_t K &= -\nabla^2 \alpha + \frac{1}{6} \alpha (9 \hat{A}_{\parallel}^2 + 2K^2) \\ &\quad + 4\pi \alpha (\rho + S_{\parallel} + 2S_{\perp}), \end{aligned} \quad (11d)$$

$$\begin{aligned} \partial_t \hat{A}_{\parallel} &= -\left(\nabla^r \nabla_r \alpha - \frac{1}{3} \nabla^2 \alpha \right) + \alpha \left(R_r^r - \frac{1}{3} R \right) \\ &\quad + \alpha K \hat{A}_{\parallel} - \frac{16}{3} \pi \alpha (S_{\parallel} - S_{\perp}), \end{aligned} \quad (11e)$$

$$\begin{aligned} \partial_t \hat{\Delta}^r &= -\frac{2}{\hat{\gamma}_{\parallel}} \partial_r (\alpha \hat{A}_{\parallel}) + 2\alpha \hat{A}_{\parallel} \left(\hat{\Delta}^r - \frac{3}{r \hat{\gamma}_{\perp}} \right) \\ &\quad + \frac{\alpha \xi}{\hat{\gamma}_{\parallel}} M_r. \end{aligned} \quad (11f)$$

In order to simplify the notation we have introduced the quantities $S_{\parallel} := S_r^r$ and $S_{\perp} := S_\theta^\theta = S_\varphi^\varphi$, with the momentum density given by $j^i = (j^r, 0, 0)$. In the last equation above ξ is an arbitrary constant which must be such that $\xi > 1/2$ in order for the evolution system to be strongly hyperbolic. An optimal choice is $\xi = 2$, which eliminates the divergence of \hat{A}_{\parallel} from the evolution equation for $\hat{\Delta}^r$, and can also be shown to imply that all propagating modes not directly related to the gauge choice do so at the coordinate speed of light. This is the value that we use in all the simulations below.¹

¹ In spherical symmetry there are no gravitational waves, so all propagating modes are either pure gauge modes, or modes associated with the constraints, neither of which represents the

We shall also recast the matter field equations as a first order in time system that we will solve simultaneously with the geometric equations above; see Sections V and VI below for our particular cases. Special care should be taken when solving hydrodynamic scenarios since they inherently develop shocks. In that case it is convenient to recast the equations in a conservative form and apply high resolution shock-capturing schemes [48].

The formulation summarized above is well suited to standard numerical techniques. In the code OllinSphere2 we discretize the spatial derivative operators up to fourth order using standard centered differences, and evolve forward in time using a method of lines with a fourth order Runge-Kutta integration scheme. The coordinate singularity associated with the origin in spherical symmetry is dealt with by staggering the origin and defining auxiliary dynamical functions that allow us to impose adequate regularity conditions [19]. To improve stability during the simulations we also add Kreiss-Oliger numerical dissipation terms to the evolution equations [49].

Finally, in order to find suitable initial data that satisfy the constraints we employ different techniques depending on the scenario we are studying, as will be explained in the sections below.

III. COSMOLOGICAL EVOLUTIONS I: THE HOMOGENEOUS AND ISOTROPIC UNIVERSE

A first step in order to perform numerical evolutions of nontrivial matter distributions is to be able to reproduce the dynamics of a homogeneous and isotropic background using the same algorithms. This approach has been used previously in three dimensions to compare numerical homogeneous spacetimes with their corresponding analytical solutions [50]. It is somewhat trivial since in a homogeneous scenario all the spatial derivatives vanish, and a consistent numerical implementation then reduces to solving the same set of ordinary differential equations at every grid point. Nevertheless, once we drop the homogeneous assumption we will need to solve the full system and our methods will be optimal.

At this point we need to specify our gauge choice for the foliation, that is, our “slicing condition” (remember that we are assuming that the shift vector vanishes). The simplest choice would be to take a constant lapse, $\alpha = 1$, which corresponds to the standard “synchronous gauge” used in cosmology. In this case the coordinates are comoving with the expansion of the universe, with the time function t representing the proper time measured by the comoving observers. One should be very cautious about this gauge choice since it is well-known that in more gen-

eral situations (black hole mergers, gravitational collapse, compact objects) this choice of lapse, commonly known as “geodesic slicing” in the numerical relativity literature, tends to focus coordinate lines, which in turn leads to coordinate singularities that quickly spoil the simulations (see *e.g.* Ref. [20] for details). Furthermore, this choice formally spoils the strong hyperbolicity properties of the evolution system, so it is undesirable for studying the local dynamics of the gravitational field.

A better alternative is to extend our analysis by considering a more general foliation of the Bona-Masso family [51],

$$\partial_t \alpha = -\alpha^2 f(\alpha) K, \quad f(\alpha) > 0. \quad (12)$$

The properties of this foliation depend on the choice of the function $f(\alpha)$: choosing $f = 0$ reduces to the case of geodesic slicing, *i.e.* the synchronous gauge; taking instead $f = 1$ turns out to be equivalent to asking for the time coordinate to be a harmonic function of spacetime and is known as “harmonic slicing”; finally, choosing $f = 2/\alpha$ corresponds to the standard “1+log” foliation commonly used in black hole evolutions.

Since for the configurations we will be considering in this paper the extrinsic curvature acquires a negative background value away from the perturbations (we will be interested in the study of expanding universes), the lapse function given in Eq. (12) will be monotonically growing in those regions, and we must control this behavior in order for our simulations to remain stable. It turns out that choosing $f(\alpha)$ to be a constant with $f < 1/3$ keeps the background coordinate speed of light $v_c = \alpha/\psi^2$ always less than unity, which allows us to fulfill the Courant stability condition. In the limiting case $f = 1/3$ one recovers the usual “conformal time slicing” $\alpha = \psi^2$ for the homogeneous evolutions (more generally, taking $f(\alpha)$ constant one finds $\alpha = \psi^{6f}$). For the results presented in this work we will limit our choice to $f \simeq 1/3$ in order to compare with known results, but for the following discussion a particular lapse is not assumed. (For practical purposes our coordinate time t may be identified with the usual cosmological conformal time η , that is $t = \eta$, but with the Big Bang not occurring necessarily at $\eta = 0$ as explained below.)

In order to proceed we need to find initial data representing homogeneous and isotropic distributions of matter. In any gauge with vanishing shift vector that corresponds to

$$\rho(t = t_0, r) = \bar{\rho}_0, \quad (13a)$$

$$j_r(t = t_0, r) = 0, \quad (13b)$$

$$S_{\parallel}(t = t_0, r) = \bar{S}_{\parallel 0}, \quad (13c)$$

$$S_{\perp}(t = t_0, r) = \bar{S}_{\perp 0} = \bar{S}_{\parallel 0}, \quad (13d)$$

with $\bar{\rho}_0$ and $\bar{S}_{\parallel 0}$ constants (note that the equations for the matter fields can introduce some relations between these two quantities). From now on the subscript zero will make reference to values measured at $t = t_0$, whereas the

propagation of physical information. Still, having the modes associated with the constraints propagating at the coordinate speed of light is advantageous from the numerical point of view.

over-bar denotes background quantities. That distinction will be relevant later for the description of nontrivial matter distributions.

The constraint equations (10) can be satisfied identically at $t = t_0$ if we choose

$$\bar{K}_0^2 = 24\pi\bar{\rho}_0, \quad \bar{R}_0 = \bar{A}_{||0} = 0. \quad (14)$$

The initial metric components $\bar{\chi}_0$, $\bar{\gamma}_{||0}$, $\bar{\gamma}_{\perp 0}$, and $\bar{\alpha}_0$ are constants but otherwise arbitrary. With no loss of generality we can fix $\bar{\chi}_0 = 0$ (*i.e.* $\bar{\psi}_0 = 1$), and $\bar{\gamma}_{||0} = \bar{\gamma}_{\perp 0} = \bar{\alpha}_0 = 1$. The condition $\bar{R}_0 = 0$ guarantees that the spatial hypersurface at $t = t_0$ is flat, so that $\bar{\Delta}_0^r = 0$.

Introducing the above initial data into the evolution equations (11) we find that during the whole evolution we must have

$$\bar{\gamma}_{||} = \bar{\gamma}_{\perp} = 1, \quad \bar{A}_{||} = \bar{\Delta}^r = 0. \quad (15)$$

On the other hand the conformal factor, the trace of the extrinsic curvature and the lapse function must satisfy the ordinary differential equations

$$\partial_t \bar{\chi} = -\frac{1}{6} \bar{\alpha} \bar{K}, \quad (16a)$$

$$\partial_t \bar{K} = \frac{1}{3} \bar{\alpha} \bar{K}^2 + 4\pi \bar{\alpha} (\bar{\rho} + \bar{S}), \quad (16b)$$

$$\partial_t \bar{\alpha} = -\bar{\alpha}^2 f(\bar{\alpha}) \bar{K}, \quad (16c)$$

together with the Hamiltonian constraint (the momentum constraint is now trivial)

$$\bar{K}^2 = 24\pi\bar{\rho}. \quad (16d)$$

Clearly $\bar{\chi}$, \bar{K} , and $\bar{\alpha}$ are functions of time only. Note that \bar{S} is the trace of the stress tensor, which in the case of a perfect fluid is just three times the value of the pressure measured by the observers at rest with respect to the fluid, $\bar{S} = 3\bar{p}$.

Of course Eqs. (16) are just the standard Friedmann equations in disguise. In order to see that it is in fact more convenient to look at them in terms of the comoving time, $\tau = \int \bar{\alpha} dt$, where the evolution of the lapse function decouples and the other three equations simplify to ²

$$\partial_\tau \bar{\chi} = -\frac{1}{6} \bar{K}, \quad (17a)$$

$$\partial_\tau \bar{K} = \frac{1}{3} \bar{K}^2 + 4\pi (\bar{\rho} + \bar{S}), \quad (17b)$$

$$\bar{K}^2 = 24\pi\bar{\rho}. \quad (17c)$$

From the three equations above we can easily identify the scale factor a and Hubble parameter $H := \partial_\tau a/a$,

$$a = \bar{\psi}^2, \quad H = 2\partial_\tau \bar{\chi} = -\bar{K}/3. \quad (18)$$

² Another interesting possibility would be to use conformal time, $\eta = \int \bar{\alpha}/\bar{\psi}^2 dt$, as we will do later in Section IV.

It should be noted that in order to have initial data representing an expanding universe one must choose the trace of the extrinsic curvature to have a negative initial value, $\bar{K}_0 = -3H_0 < 0$.

To close the system we still need to specify the evolution equations for the matter fields, as we will do later for the case of a perfect fluid, Section V, and a scalar field, Section VI.

IV. COSMOLOGICAL EVOLUTIONS II: THE PERTURBATIONS

If we leave the symmetries of the homogeneous and isotropic background aside (but still preserving the invariance under rotations about the origin), the initial data in Eqs. (13) can be generalized to

$$\rho(t = t_0, r) = \rho_0(r), \quad (19a)$$

$$j_r(t = t_0, r) = j_{r0}(r), \quad (19b)$$

$$S_{||}(t = t_0, r) = S_{||0}(r), \quad (19c)$$

$$S_{\perp}(t = t_0, r) = S_{\perp 0}(r). \quad (19d)$$

Without loss of generality, we will also consider that the momentum density vanishes at $t = t_0$, *i.e.* $j_0^r(r) = 0$. This particular choice implies that the matter is initially following the expansion at the initial slice.

In order to compare our numerical simulations with previous analytical results (obtained to linear order in a perturbation series), we will consider the evolution of initial data that are not exactly homogeneous and isotropic, but are very close to it. That is, we assume that for any physical quantity $f(t, r)$ evaluated at $t = t_0$ we can always write

$$f_0(r) = \bar{f}_0 + \delta f_0(r), \quad (20)$$

with $|\delta f_0(r)| \ll |\bar{f}_0|$. In our simulations the functions $\delta f_0(r)$ at $t = t_0$ have either compact support on a finite region, or decay very rapidly for large r . We can then safely identify \bar{f}_0 with the value of the function $f_0(r)$ at the numerical boundary. We will also choose the boundary of the computational domain to be sufficiently distant so that the perturbations never reach it during the simulation.

If we choose an initial slice with constant expansion $\bar{K}_0^2 = 24\pi\bar{\rho}_0$, together with $\bar{A}_{||0} = 0$, the momentum constraint (10b) is still trivially satisfied, while the Hamiltonian constraint (10a) takes the form

$$R_0 - 16\pi(\delta\rho_0) = 0. \quad (21)$$

The perturbation in the energy density, $\delta\rho_0$, now implies that the initial spatial hypersurface cannot be flat. The three dimensional Ricci scalar takes the general form $R = \hat{R}/\psi^4 - 8(\hat{\nabla}^2\psi)/\psi^5$. We can choose the spatial metric to be initially conformally flat, so that $\hat{\gamma}_{||0} = \hat{\gamma}_{\perp 0} = 1$, $\hat{\Delta}_0^r = 0$, and $\hat{R}_0 = 0$. The Hamiltonian

constraint then reduces to the following elliptic equation for the conformal factor,

$$\hat{\nabla}^2 \psi_0 + 2\pi(\delta\rho_0)\psi_0^5 = 0. \quad (22)$$

In spherical symmetry this is just a second-order ordinary differential equation. There are two linearly independent solutions to Eq. (22); however, regularity at the origin and an asymptotic decay to the background value,

$$\partial_r \psi_0(r=0) = 0, \quad \psi_0(r \rightarrow \infty) = 1, \quad (23)$$

singles out the physical solution. Note that if the perturbation vanishes everywhere, $\delta\rho_0(r) = 0$, then $\psi_0(r) = 1$, and we recover the background expression of the conformal factor.

To evaluate the perturbation $\delta f(t, r)$ of a given dynamical quantity at any time $t > t_0$ in the evolution we simply remove from the field $f(r)$ its value at the numerical boundary, where the effect of the inhomogeneity has not arrived yet. Of course we can do this only for a finite amount of evolution time, but as we have argued previously this will be sufficient for the purposes of this paper.

Some words about how to compare our simulations with the standard cosmological treatment of linear perturbations are in order here. In cosmology the metric tensor of a flat Friedmann universe with small perturbations is usually parametrized in the form³

$$\begin{aligned} ds^2 = & a^2 \left[-(1 + 2\Phi) d\eta^2 - 2\partial_i B dx^i d\eta \right. \\ & + (1 - 2\Psi - 2\partial_r^2 E) dr^2 \\ & \left. + (1 - 2\Psi - (2/r) \partial_r E) r^2 d\Omega^2 \right]. \quad (24) \end{aligned}$$

We restrict our attention to the scalar sector of the perturbations: vector and tensor modes cannot be excited in a spherically symmetric configuration and for that reason they have not been included here. Under these assumptions the fields Φ , B , Ψ and E in Eq. (24) measure the small deviations of a spacetime with respect to an exact flat homogeneous and isotropic universe.

The spacetime length-element in the numerical code, on the contrary, can be expressed in the form

$$ds^2 = a^2 \left[-\frac{\psi^4}{a^2} d\eta^2 + \frac{\psi^4}{a^2} (\hat{\gamma}_{\parallel} dr^2 + \hat{\gamma}_{\perp} r^2 d\Omega^2) \right]. \quad (25)$$

Here the scale factor is identified from the background universe, Eq. (18) above, with $\eta = \int \bar{\alpha}/\bar{\psi}^2 dt$ the cosmological time in conformal coordinates as a function of the time coordinate t of the code. Comparing Eqs. (24) and (25) we can easily identify $1 + 2\Phi = e^{4\delta\chi}$, $B = 0$,

$1 - 2\Psi - 2\partial_r^2 E = e^{4\delta\chi} \hat{\gamma}_{\parallel}$, and $1 - 2\Psi - (2/r)\partial_r E = e^{4\delta\chi} \hat{\gamma}_{\perp}$. Working to first-order in the perturbations, and after some algebra, we finally obtain

$$\Phi = 2\delta\chi, \quad (26a)$$

$$B = 0, \quad (26b)$$

$$\Psi = -\int^r \frac{dr_1}{2r_1} (\delta\hat{\gamma}_{\perp} - \delta\hat{\gamma}_{\parallel}) - \frac{1}{2}\delta\hat{\gamma}_{\perp} - 2\delta\chi, \quad (26c)$$

$$E = \int^r r_2 dr_2 \int^{r_2} \frac{dr_1}{2r_1} (\delta\hat{\gamma}_{\perp} - \delta\hat{\gamma}_{\parallel}). \quad (26d)$$

The constants of integration in Eqs. (26c) and (26d) are fixed in order to have regular values of Ψ and E that match the homogeneous background at the boundary. Remember that we previously fixed the shift vector to zero and for that reason the field B vanishes.

Note that the perturbations in the metric tensor as defined in Eqs. (24) and (26) depend on the particular choice of coordinates. However, it is always possible to define a set of gauge-invariant functions of the form

$$\Phi_{\text{g.i.}} = \Phi - (1/a) [a(B - E')]', \quad (27a)$$

$$\Psi_{\text{g.i.}} = \Psi + \mathcal{H}(B - E'), \quad (27b)$$

that do not change under general (first order) coordinate transformations. Here the prime denotes the derivative with respect to the conformal time, and $\mathcal{H} := a'/a$.⁴ A similar expression for a gauge-invariant perturbation in the energy density takes the form

$$\delta\rho_{\text{g.i.}} = \delta\rho - \bar{\rho}'(B - E'). \quad (28)$$

Equations (27) and (28) were reported for the first time by Bardeen in Ref. [52], and since then they have been frequently used to characterize cosmological linear order perturbations. They involve derivatives with respect to the conformal time, so that then they are in fact numerically nontrivial. However, they can be written explicitly in terms of other fields by means of the evolution equations. In particular, for the time derivatives of the perturbations in the metric tensor we obtain, up to linear order,

$$E' = \frac{3}{2} \bar{\psi}^2 \int^r r_2 dr_2 \int^{r_2} \frac{dr_1}{r_1} \hat{A}_{\parallel}, \quad (29a)$$

$$E'' = \frac{3}{2} \frac{\bar{\psi}^4}{\bar{\alpha}} \int^r r_2 dr_2 \int^{r_2} \frac{dr_1}{r_1} \left(\partial_t \hat{A}_{\parallel} - \frac{1}{3} \bar{\alpha} \bar{K} \hat{A}_{\parallel} \right). \quad (29b)$$

The explicit form of $\bar{\rho}'$ can be found in a similar way once the matter fields are specified.

³ See for instance Section 7.1 in Ref. [3]. Note however that we use a different signature for the spacetime metric, and a coordinate system adapted to the spherical symmetry.

⁴ In this paper we will consider matter fields that do not develop anisotropic stresses (to linear order); this guarantees that $\Phi_{\text{g.i.}} = \Psi_{\text{g.i.}}$ (to this same order in the perturbation series). The field $\Phi_{\text{g.i.}}$ is analogous to the gravitational potential in the non-relativistic theory and for that reason it is usually known as the Newtonian potential.

At this point it is important to emphasize once again that the code OllinSphere2 evolves initial data in terms of some dynamical fields $f(t, r)$, and it does not distinguish between background values, $\bar{f}(t)$, and their perturbations, $\delta f(t, r)$; see for instance Eqs. (10) and (11) above. However, the definitions in this section are convenient in order to compare the numerical evolutions presented here with previous analytical results obtained when “the perturbations are not to large”, as we will do next in Section V for the case of a pressureless perfect fluid.

V. PRESSURELESS PERFECT FLUID (DUST)

At large scale dark matter is usually described in terms of a perfect fluid with equation of state $p = 0$, known generically as “dust” in relativity. The energy-momentum tensor of a perfect fluid with no pressure takes the form $T_{\mu\nu} = \rho_{\text{rest}} u_\mu u_\nu$, where u_μ is the four-velocity of the fluid elements and $\rho_{\text{rest}} := T_{\mu\nu} u^\mu u^\nu$ is the energy density measured by the observers comoving with the fluid. Note that, in general, the energy density measured by the observers at rest with respect to the fluid does not coincide with the energy density measured by the Eulerian observers, Eq. (3a).

For the case of a universe dominated by a perfect fluid with vanishing pressure there is in fact an analytic expression for the scale factor as a function of the conformal cosmological time,⁵

$$a(\eta) = a_0 \left(\frac{\eta}{\eta_{\text{BB}}} - 1 \right)^2, \quad (30)$$

as well as for the gauge-invariant perturbations in the metric tensor,

$$\begin{aligned} \Phi_{\text{g.i.}}(\eta, \vec{x}) &= \Psi_{\text{g.i.}}(\eta, \vec{x}) \\ &= C_1(\vec{x}) + C_2(\vec{x}) \left(\frac{\eta}{\eta_{\text{BB}}} - 1 \right)^{-5}, \end{aligned} \quad (31a)$$

and the contrast in the energy density,

$$\begin{aligned} \frac{\delta \rho_{\text{g.i.}}}{\bar{\rho}}(\eta, \vec{x}) &= \frac{1}{6} \left\{ \left[\Delta C_1(\vec{x}) (\eta - \eta_{\text{BB}})^2 - 12 C_1(\vec{x}) \right] \right. \\ &\left. + \left[\Delta C_2(\vec{x}) (\eta - \eta_{\text{BB}})^2 + 18 C_2(\vec{x}) \right] \left(\frac{\eta}{\eta_{\text{BB}}} - 1 \right)^{-5} \right\}. \end{aligned} \quad (31b)$$

Here the origin of conformal time $\eta = 0$ has been chosen arbitrarily, with the the singularity at the Big Bang fixed to $\eta = \eta_{\text{BB}} = -[3/(2\pi a_0^2 \bar{\rho}_0)]^{1/2}$. Also, $C_1(\vec{x})$ and $C_2(\vec{x})$ are arbitrary functions of the spatial coordinates that depend on the initial perturbations and can be determined

from the initial data through

$$C_1(\vec{x}) = \Psi_{\text{g.i.}}(0, \vec{x}) - \frac{\eta_{\text{BB}}}{5} \Psi'_{\text{g.i.}}(0, \vec{x}), \quad (32a)$$

$$C_2(\vec{x}) = -\frac{\eta_{\text{BB}}}{5} \Psi'_{\text{g.i.}}(0, \vec{x}). \quad (32b)$$

Notice that, after some transient time, the Newtonian potential remains constant, $\Phi_{\text{g.i.}} = \Psi_{\text{g.i.}} \sim C_1(\vec{x})$. The behavior of the contrast in the energy density, on the other hand, depends on the size of the perturbations. Those modes shorter than the Hubble radius, $kr_H \gg 1$, grow in time as $(\eta - \eta_{\text{BB}})^2$ (the square of the comoving Hubble radius $r_H \equiv 1/\mathcal{H} = (\eta - \eta_{\text{BB}})/2$), whereas Fourier modes that are initially larger than the Hubble radius, $kr_H(\eta = 0) \ll 1$, remain essentially frozen until the horizon reaches them.

To deal with the numerical integration of the fluid-dynamical equations forward in time, our code has an implementation of the “Valencia formulation” of general relativistic hydrodynamics [48, 53], where the fluid dynamical variables are given in terms of the so called “conserved quantities”

$$D := \rho_{\text{rest}} W, \quad (33a)$$

$$\mathcal{S}^i := \rho_{\text{rest}} h W^2 v^i, \quad (33b)$$

$$\mathcal{E} := \rho_{\text{rest}} h W^2 - p - D. \quad (33c)$$

In these expressions $h := 1 + \epsilon + p/\rho_{\text{mass}}$ is the specific enthalpy, with ρ_{mass} the rest mass density and ϵ the specific internal energy defined as $\epsilon := \rho_{\text{rest}}/\rho_{\text{mass}} - 1$. We have also introduced the variable $W := -u^\mu n_\mu = \alpha u^0 = 1/\sqrt{1 - \gamma_{ij} v^i v^j}$, which is just the Lorentz factor associated with the velocity of the fluid elements v^i measured by the Eulerian observers. The conserved quantities have the following physical interpretation: D is the rest mass density measured by the Eulerian observers, \mathcal{S}^i is the momentum density measured by the same observers, while \mathcal{E} is the difference between the total energy density and the rest mass density measured in the same Eulerian frame, $\mathcal{E} = \rho - D$. We have defined the conserved quantities for the general case of nonzero pressure; however, notice that for a pressureless fluid we will in fact have $p = 0$ and $\rho_{\text{mass}} = \rho_{\text{rest}}$, so that $\epsilon = 0$ and $h = 1$.

An important issue in the Valencia formulation of relativistic hydrodynamics is the fact that the conversion from the primitive variables ($\rho_{\text{rest}}, \epsilon, v^i$) to the conserved quantities ($D, \mathcal{E}, \mathcal{S}^i$) is given in terms of transcendental equations. However, for the situation of interest here this is not relevant since for dust we have $p = 0$, $\epsilon = 0$, and $h = 1$, so that

$$v^i = \mathcal{S}^i / (\mathcal{E} + D), \quad \rho_{\text{rest}} = D/W. \quad (34)$$

In terms of the conserved quantities, the evolution equations for a pressureless perfect fluid can be written

⁵ See *e.g.* Eqs. (1.77), (7.53), and (7.54) in Ref. [3].

in conservative form as

$$\partial_t D - \mathcal{L}_{\bar{\beta}} D = -\nabla_k (\alpha D v^k) + \alpha K D, \quad (35a)$$

$$\begin{aligned} \partial_t \mathcal{S}^i - \mathcal{L}_{\bar{\beta}} \mathcal{S}^i &= -\nabla_k (\alpha \mathcal{S}^i v^k) + \alpha K \mathcal{S}^i \\ &\quad - (\mathcal{E} + D) \nabla^i \alpha, \end{aligned} \quad (35b)$$

$$\begin{aligned} \partial_t \mathcal{E} - \mathcal{L}_{\bar{\beta}} \mathcal{E} &= -\nabla_k (\alpha \mathcal{E} v^k) + \alpha K \mathcal{E} \\ &\quad + (\mathcal{E} + D) (\alpha v^m v^n K_{mn} - v^m \partial_m \alpha). \end{aligned} \quad (35c)$$

On the other hand, the sources of the gravitational field given in Eqs. (3) and (5) take a particularly simple form for a pressureless fluid,

$$\rho = \mathcal{E} + D, \quad (36a)$$

$$j^i = \mathcal{S}^i, \quad (36b)$$

$$S_{ij} = v_i \mathcal{S}_j. \quad (36c)$$

Our numerical code integrates, in spherical symmetry, these equations forward in time simultaneously with the integration of the spacetime variables. While the spacetime integration can be dealt with a simple method of lines, the equations for the fluid are integrated with advanced shock-capturing numerical methods (see *e.g.* [54]).

As already mentioned, we perform all our simulations with a vanishing shift vector and a slicing condition of the Bona-Masso family, Eq. (12). In particular, we chose $f = 0.3332$ in order to be close to the case that reduces to the conformal time slicing for a homogeneous distribution. Taking this into account we can compare directly the result of our evolutions with the analytical expressions such as those in Eqs. (30) and (31). We use a numerical grid of 10^4 points, with a spacing of $\Delta r = 0.1$.

For the case of a perfect fluid with no pressure and vanishing initial velocity with respect to the comoving coordinates, $v^r(t = t_0) = 0$, the initial data of Eqs. (19) simplifies to

$$\rho(t = t_0, r) = \rho_0(r), \quad (37a)$$

$$j^r(t = t_0, r) = 0, \quad (37b)$$

$$S_{\parallel}(t = t_0, r) = 0, \quad (37c)$$

$$S_{\perp}(t = t_0, r) = 0. \quad (37d)$$

Notice that since initially $v^r = 0$, the energy density measured by the Eulerian observers coincides with the one measured by the observers comoving with the fluid, so that $\rho_0(r) = \rho_{\text{rest}0}(r) = D_0(r)$, $S_0^r = \mathcal{E}_0 = 0$.

Once the initial profile for the energy density $\rho_0(r)$ is given, and it is decomposed into a background and a perturbation,

$$\rho_0(r) = \bar{\rho}_0 + \delta\rho_0(r), \quad (38a)$$

all that one needs to do is to specify an initial geometry consistent with such a matter distribution, as we learned previously in Sections III and IV. In order to construct initial data corresponding to a localized inhomogeneity living in an expanding, otherwise homogeneous

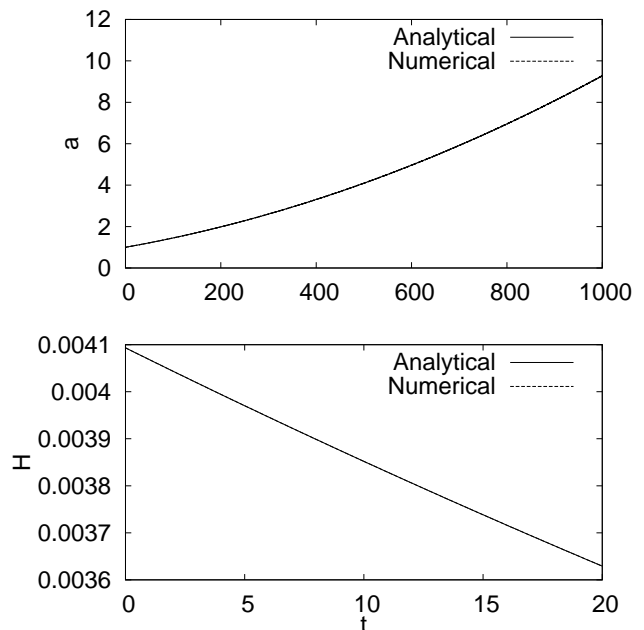


FIG. 1: Evolution of the scale factor a (top panel) and Hubble parameter H (bottom panel), as functions of coordinate time t , for an expanding homogeneous and isotropic universe dominated by a perfect fluid with no pressure (dust). Here we have chosen $\rho_0 = 2 \times 10^{-6}$ and $\delta\rho_* = 0$. We show both the numerical evolution (dotted-line), and the analytic solution of Eq. (30) (solid-line). The scale is zoomed in near the origin for the bottom panel in order to appreciate the detail and for comparison below.

and isotropic universe, we parametrize the initial perturbation of the energy density as

$$\delta\rho_0(r) = \delta\rho_* \left(1 - \frac{11r^2}{3L^2}\right) \left[\left(1 - \frac{r}{L}\right) \left(1 + \frac{r}{L}\right)\right]^3, \quad (38b)$$

for $0 < r < L$, and $\delta\rho_0(r) = 0$ for $r \geq L$. Here $\delta\rho_*$ and L are an amplitude and a length-scale for the initial perturbation, respectively (see for instance the first panels in Figures 3 and 5 below for particular realizations). We have chosen such a parametrization in order to guarantee that the perturbation has both compact support and integrates to zero, $\int_V \delta\rho_0(r) d^3\vec{x} = 0$. Our motivation here is that the perturbation should correspond to a redistribution of matter within a flat universe, and not to an addition of extra matter. As long as $\delta\rho_* \ll \bar{\rho}_0$ we should have a cosmological evolution that can be well described in terms of linear perturbation theory, Eqs. (31) above, at least for a finite period of time until the nonlinear evolution becomes relevant.

Figure 1 shows, for the case of a homogeneous and isotropic universe with $\bar{\rho}_0 = 2 \times 10^{-6}$ and $\delta\rho_* = 0$, a comparison of the evolution of the scale factor obtained with our numerical implementation against the analytical solution for a Friedmann universe given in Eq. (30). Since we are interested in the case of an expanding configuration we need to choose the negative root of the trace

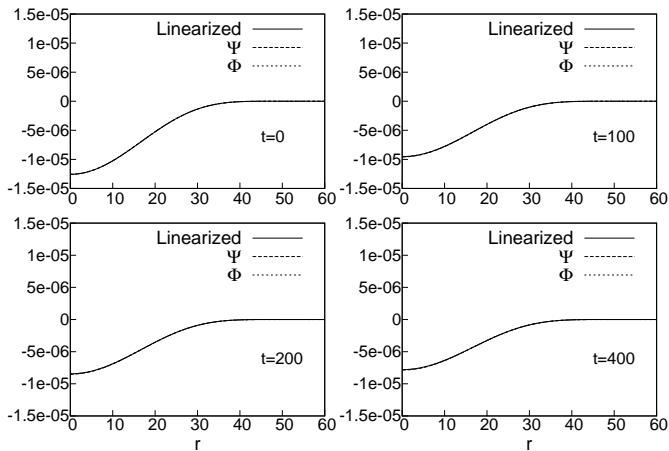


FIG. 2: Snapshots of the evolution of the gauge-invariant perturbations in the metric tensor, $\Phi_{\text{g.i.}}$ and $\Psi_{\text{g.i.}}$, as functions of the comoving radial coordinate, r . Here we have chosen initial data of the form in Eq. (38) with $\bar{\rho}_0 = 2.0 \times 10^{-6}$, $\delta\rho_* = 1.2 \times 10^{-8}$ and $L = 50$. We show the results of the numerical evolution, $\Psi_{\text{g.i.}}$ (dotted-line), $\Phi_{\text{g.i.}}$ (dashed-line), together with the analytic solution obtained in the linear regime, Eq. (31a), (solid-line).

of the extrinsic curvature, $K_0 = -1.228 \times 10^{-2}$. As can be seen from the figure, the numerical result is very accurate and converges consistently with the discretization order of the integration method.⁶

We analyze now the evolution of the perturbed case. For this scenario we have chosen an initial background density of $\bar{\rho}_0 = 2.0 \times 10^{-6}$, with an amplitude for the perturbation of $\delta\rho_* = 1.2 \times 10^{-8}$. We have fixed the characteristic length-scale in Eqs. (38) to $L = 50$. The parameters have been chosen in order to have a perturbation whose length-scale is well inside the Hubble radius, with an initial contrast in the energy density that allows us to compare the numerical evolutions with the analytic results obtained in the linear regime.

In Figure 2 we show the numerical evolution of the gauge-invariant metric perturbations, $\Phi_{\text{g.i.}}$ and $\Psi_{\text{g.i.}}$, along with the evolution expected from the linear order analysis, Eq. (31a). The functions $C_1(\vec{x})$ and $C_2(\vec{x})$ in Eq. (31a) have been determined from the initial data using the expressions in Eqs. (32). Throughout the whole evolution the relation $\Psi_{\text{g.i.}} = \Phi_{\text{g.i.}}$ is satisfied up to nu-

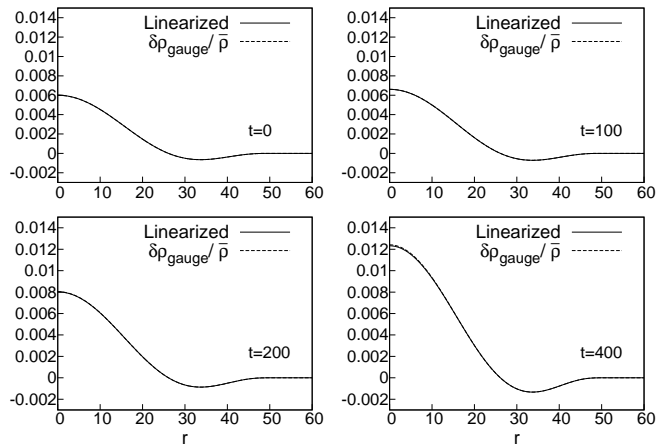


FIG. 3: Snapshots of the contrast in the energy density, $\delta\rho_{\text{g.i.}}/\bar{\rho}$, for the same initial data as in Figure 2. We show the results of the numerical evolution (dashed-line), together with the analytic solution obtained in the linear regime, Eq. (31b), (solid-line).

merical error, and converges consistently with the discretization order. Also, the numerical results coincide remarkably well with those predicted by the analytic expressions obtained in the linear regime. Note that after some time, in this case at $t \sim 300$, the Newtonian potential approaches its asymptotic value $C_1(\vec{x})$.

Figure 3 shows, for the same initial data as in Figure 2, the numerical evolution of the contrast in the energy density, $\delta\rho_{\text{g.i.}}/\bar{\rho}$, and we compare it with the evolution predicted with the linear order theory, Eq. (31b). Since the characteristic size of the initial perturbation is well inside the Hubble radius, all the significant modes contributing to the inhomogeneity grow at the same rate and the profile is only rescaled as time moves forward. As can be appreciated from the figure, the evolution of the density contrast also coincides very well with the prediction obtained from the linearized theory.

Our numerical results confirm what was already known from linear theory for the behavior of small perturbations. However, in a universe dominated by dust the inhomogeneities are expected to grow indefinitely as the universe expands. This poses a problem for the linearized approximation since the natural evolution will drive the system away from this regime. In order to dive into the nonlinear regime we have performed simulations with the same background settings as those in Figures 2 and 3 above, but with a larger perturbation amplitude, $\delta\rho_* = 6 \times 10^{-7}$, in order to have an initial value for the energy density contrast of order 10^{-1} . The new simulations proceed initially in a similar way to the previous ones, see Figures 4 and 5. However, as expected, we soon find an appreciable deviation from the predictions of the linear theory. This deviation grows as time proceeds, although it is interesting to note that the regions that have not entered the nonlinear regime, $r \gtrsim 15$ in the

⁶ Numerically we work with dimensionless coordinates and quantities. In order to recover the physical quantities we need an arbitrary length-scale λ such that $x_{\text{phys}}^\mu = \lambda x^\mu$; then the numerical solutions obtained can be related to the physical ones by dividing the derivatives of the extrinsic curvature K_{ij} and connection vector $\hat{\Delta}^i$ by λ , and the matter sources ρ , j^i and S_{ij} by λ^2 . For a pressureless fluid there is not an a priori choice for this scale, which is an advantageous fact that enables us to make comparisons with other models by choosing an appropriate physical scale.

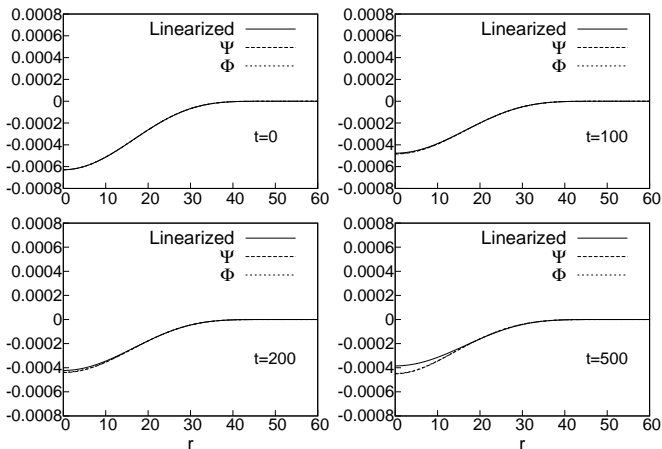


FIG. 4: Similar to Figure 2 but now for initial data with $\bar{\rho}_0 = 2.0 \times 10^{-6}$, $\delta\rho_* = 1.2 \times 10^{-7}$ and $L = 50$ in Eq. (38). Note that, after some transient time $t \sim 200$, deviations from the linearized predictions become apparent.

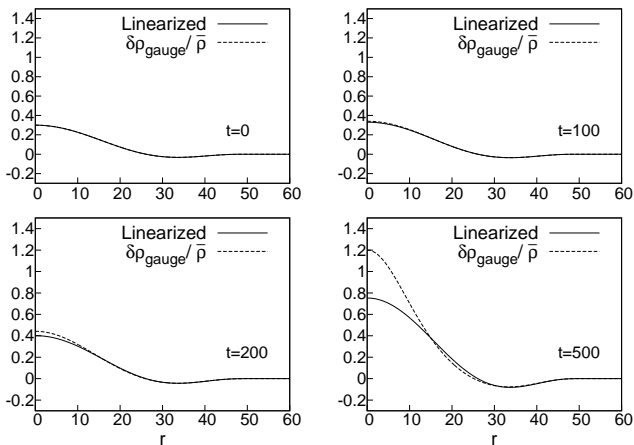


FIG. 5: Similar to Figure 3 but now for the same initial data of Figure 4. Note again that, after some transient time $t \sim 200$, deviations from the linearized predictions become apparent.

figures, are still described reasonably well by the linear order expressions.

Finally, in Figure 6 we show, for the same initial data as in Figures 4 and 5, the evolution of the central value of the potentials $\Psi_{g.i.}$ and $\Phi_{g.i.}$ as a function of the contrast in the energy density evaluated at the center of the configuration. Note that the two potentials still follow each other closely during the evolution, but their values start to differ from the linear theory prediction as time moves forward. Moreover, while in the linear approximation the central absolute value of the potentials continues to become smaller, in the nonlinear evolution this absolute value first becomes smaller, but later starts to grow again, the transition occurring roughly when the maximum of the energy contrast has reached $(\delta\rho_{g.i.}/\bar{\rho})_{\max} \sim 0.6$. It is not surprising to find a different

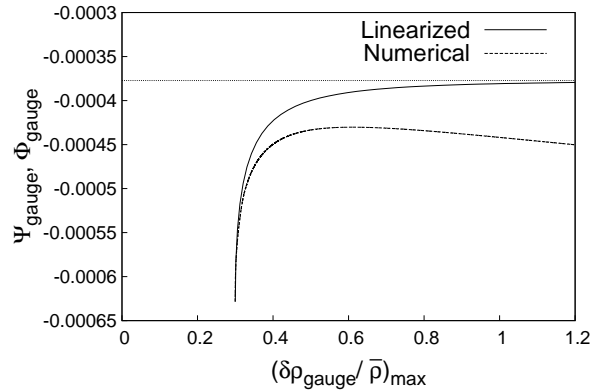


FIG. 6: Central value of the potentials $\Psi_{g.i.}$ and $\Phi_{g.i.}$ as a function of the central value of the contrast in the energy density for the same evolution as in Figures 4 and 5. The dashed line corresponds to the results of the numerical evolution, while the solid line shows the analytic solution obtained in the linear regime. The dotted line represents the asymptotic value for the linearized approximation at the origin, $C_1(r=0)$.

behavior at this level, since the gauge-invariant quantities are only well defined during the linear regime, and we should be cautious on how to extract meaningful results once the nonlinear regime has been reached. However, it is interesting to note that top-hat models of structure formation suggest that this transition should happen at a density contrast of order $(\delta\rho_{g.i.}/\bar{\rho})_{\max} \sim 1.7$, which corresponds to the moment when the core starts to collapse as a closed Friedmann universe (see for instance Section 9.3 in Ref. [55]). Our results show that, at least for the initial conditions considered here, this transition occurs well below this value.

VI. REAL MASSIVE SCALAR FIELD

In this section we consider the evolution of a universe dominated by a massive scalar field satisfying the Klein-Gordon equation,

$$(\square - m^2)\varphi = 0. \quad (39)$$

In the above equation m is the “mass parameter” of the scalar particle and has dimensions of inverse distance (it is just the inverse of the Compton wavelength of the scalar particle).⁷ The energy-momentum tensor asso-

⁷ If the fundamental particle associated with the scalar field has mass μ , then we have $m = \mu c/\hbar = 1/\lambda_C$, with λ_C the Compton wavelength, and where for the sake of clarity we have written explicitly the dependence on the speed of light c . The mass parameter therefore provides a natural length-scale for the scalar field.

ciated to a canonical, real, massive scalar field with no self-interactions takes the form

$$T_{\mu\nu} = \partial_\mu\varphi\partial_\nu\varphi - \frac{1}{2}g_{\mu\nu}(\partial_\alpha\varphi\partial^\alpha\varphi + m^2\varphi^2). \quad (40)$$

A free scalar field oscillating with high frequency (when compared to the expansion rate of the universe) around the minimum of the potential has been considered as a possible candidate to describe the dark matter content of the universe [5, 34, 35]. To leading order in H/m , the energy density of the coherent oscillations decays with the cosmological expansion as $\rho \sim 1/a^3$, with $a \sim \eta^2$ [5, 27, 56]. The linear order perturbations evolve like those of a pressureless perfect fluid, except for the fact that the dynamics of the field introduce a cutoff in the power spectrum of the density perturbations at the scale of the Compton wavelength of the scalar particle, $\lambda_C \sim 1/m$, so that modes with smaller wavelength do not grow but just disperse with decaying amplitude, as we will show below [27].

In order to test this picture we evolve numerically cosmological initial data with a scalar field as the matter content, using the same full nonlinear code that we employed in Section V. For small perturbations we corroborate the analytical results obtained using the linearized theory. Furthermore, when the perturbations reach the nonlinear regime we find that, in general, they grow at a slower rate than in the case of dust. This is expected to delay the formation of the first structures in the universe.

To deal with the numerical evolution of the scalar field we reduce the Klein-Gordon equation to a first-order form by introducing the auxiliary variables $\Pi := n^\mu\partial_\mu\varphi$ and $\Theta_i := \partial_i\varphi$. The Klein-Gordon equation can then be written as the following system of evolution equations

$$\partial_t\varphi - \mathcal{L}_{\vec{\beta}}\varphi = \alpha\Pi, \quad (41a)$$

$$\partial_t\Theta_i - \mathcal{L}_{\vec{\beta}}\Theta_i = \partial_i(\alpha\Pi), \quad (41b)$$

$$\partial_t\Pi - \mathcal{L}_{\vec{\beta}}\Pi = \alpha\Pi K - \alpha m^2\varphi + \nabla_i(\alpha\Theta^i). \quad (41c)$$

These equations are solved simultaneously with the integration of the spacetime system. In terms of the new variables the sources of the gravitational field given in Eqs. (3) and (5) take the form

$$\rho = \frac{1}{2}(\Pi^2 + \Theta_m\Theta^m + m^2\varphi^2), \quad (42a)$$

$$j_i = -\Pi\Theta_i, \quad (42b)$$

$$S_{ij} = \Theta_i\Theta_j + \frac{1}{2}(\Pi^2 - \Theta_m\Theta^m - m^2\varphi^2)\gamma_{ij}. \quad (42c)$$

For generality, the above expressions have been written for the three-dimensional case. In our code they are reduced to their spherically symmetric form, where Θ_i only has a radial component.

As we did for the case of a perfect fluid, we perform numerical evolutions with a vanishing shift vector, and a slicing condition of the Bona-Masso family with

$f = 0.3332$. Again, we consider initial data with vanishing momentum density by choosing $\Pi(t = t_0) = 0$. With these assumptions the initial data in Eqs. (19) simplify to (remember that in Section IV we already fixed $\hat{\gamma}_{\parallel 0} = 1$)

$$\rho(t = t_0, r) = \frac{1}{2}[(\psi_0^{-2}\Theta_{r0})^2 + m^2\varphi_0^2], \quad (43a)$$

$$j_r(t = t_0, r) = 0, \quad (43b)$$

$$S_{\parallel}(t = t_0, r) = \frac{1}{2}[(\psi_0^{-2}\Theta_{r0})^2 - m^2\varphi_0^2], \quad (43c)$$

$$S_{\perp}(t = t_0, r) = \frac{1}{2}[-(\psi_0^{-2}\Theta_{r0})^2 - m^2\varphi_0^2]. \quad (43d)$$

Note that for the homogeneous and isotropic configurations, $\Theta_{r0} = 0$, we recover $S_{\parallel 0} = S_{\perp 0}$, as expected from Eqs. (13) above.

Contrary to the case of dust in Section V, we now do not specify the initial profile for the energy density, $\rho_0(r)$, but rather the initial scalar field profile φ_0 . In particular, we consider initial data of the form

$$\varphi_0(r) = \bar{\varphi}_0 + \delta\varphi_0(r), \quad (44a)$$

with

$$\delta\varphi_0(r) = \delta\varphi_* \left(1 - \frac{11r^2}{3L^2}\right) \left[\left(1 - \frac{r}{L}\right)\left(1 + \frac{r}{L}\right)\right]^3 \quad (44b)$$

for $0 < r < L$, and $\delta\varphi_0(r) = 0$ otherwise. Again, the parameter L represents a length-scale for the perturbation, whereas $\delta\varphi_*$ measures the amplitude of the inhomogeneity in the scalar field, both evaluated at $t = t_0$. Notice that since the leading-order contribution to the energy density perturbation will be linear in $\delta\varphi_0$, the above choice still guarantees that to first order the density perturbation will integrate to zero (although we will have nonvanishing second-order contributions to the integral). A geometry consistent with this initial distribution of matter is obtained following the recipes of Sections III and IV.

Figure 7 shows, for a scalar field of mass $m = 1$ and initial data $\bar{\varphi}_0 = 2 \times 10^{-3}$, $\delta\varphi_* = 0$, a comparison of the evolution of the scale factor obtained with our numerical implementation against the analytical solution for a Friedmann universe dominated by dust, Eq. (30). In this case the scalar field has already settled to oscillate near the minimum of potential, and drives the evolution of the scale factor in a way that mimics very well the behavior obtained in the case of dust, Figure 1 above. Nevertheless, on short time-scales there are small oscillations (of order H/m) of the dynamical quantities around the dust solution. These oscillations are better appreciated on the Hubble factor (see the lower panel in Figure 7). Apart from the small oscillations the two solutions coincide up to discretization error.

To analyze the behavior of the small perturbations we need to consider two different scales relative to the Compton wavelength of the scalar particle. Short-scaled perturbations (whose characteristic lengths are of order

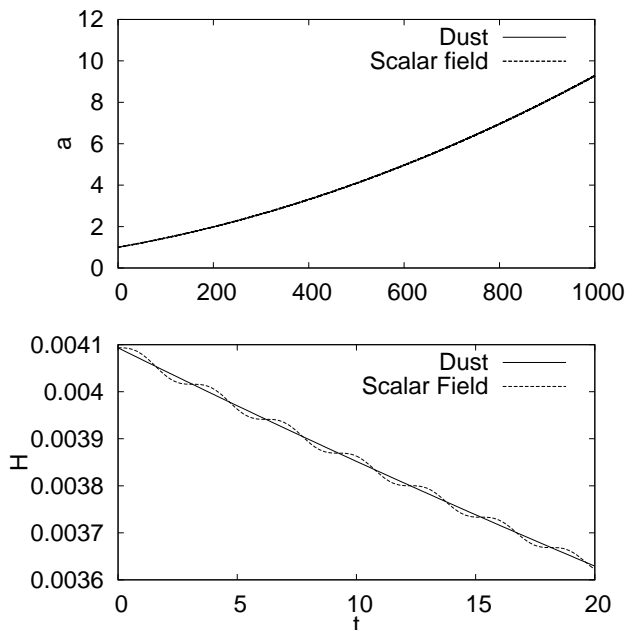


FIG. 7: Evolution of the scale factor a (top panel) and Hubble parameter H (bottom panel), as functions of coordinate time t , for an expanding homogeneous and isotropic universe dominated by the coherent oscillations of a massive scalar field (dotted line). Here we have chosen $\varphi_0 = 2 \times 10^{-3}$ and $\delta\varphi_* = 0$ in order to have the same initial configuration for the scale factor as in Figure 1. We also show the analytic expression for the case of dust, Eq. (30) (solid line). The scale is zoomed in near the origin for the bottom panel in order to appreciate the oscillations of the universe containing the scalar field.

$L \lesssim 1/m$) are composed mostly of modes shorter than the Compton wavelength. These modes propagate freely like (almost) a massless scalar field, and these perturbations are not expected to collapse unless their initial amplitude is very large. As an example of this behavior, in Figures 8 and 9 we show the numerical evolution of the gauge-invariant perturbations in the metric tensor, $\Phi_{g.i.}$ and $\Psi_{g.i.}$, and the energy density contrast, $\delta\rho_{g.i.}/\bar{\rho}$, for a scalar field with an initial data characterized by the parameters $\bar{\varphi}_0 = 2 \times 10^{-3}$, $\delta\varphi_* = 10^{-5}$, and $L = 2$. We see that basically the whole initial perturbation disperses leaving at $t = 15$ only a tiny imprint on the physical quantities measuring the inhomogeneities.

On the other hand, large-scaled perturbations with $L \gg 1/m$ have a significant contribution from modes larger than the Compton wavelength. These modes grow in a very similar way to those in a universe dominated by dust [27]. In Figures 10 and 11 we show, for initial data with the same values of $\bar{\varphi}_0$ and $\delta\varphi_*$ as in Figures 8 and 9 but with $L = 150$, the evolution of the gauge invariant perturbations of the metric and the energy density contrast, respectively, together with the predictions of the linearized theory for the case of dust. Note that in both figures the numerical evolution for the case of the scalar field coincides with that expected for dust.

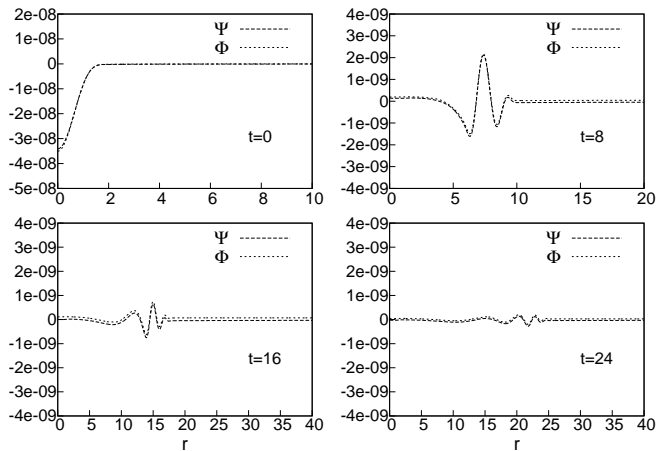


FIG. 8: Snapshots of the gauge-invariant perturbations in the metric tensor, $\Phi_{g.i.}$ and $\Psi_{g.i.}$, as a function of the comoving radial coordinate, r , at different instants of time in the cosmological evolution. Here we have chosen an initial data of the form in Eq. (44) with $\bar{\varphi}_0 = 2.0 \times 10^{-3}$, $\delta\varphi_* = 10^{-5}$, and $L = 2$. Note that the inhomogeneity is composed mostly of short wavelength modes that disperse away.

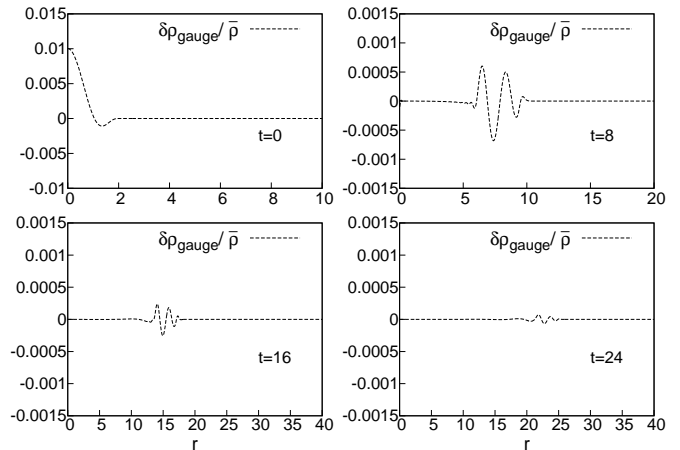


FIG. 9: Snapshots of the energy density contrast, $\delta\rho_{g.i.}/\bar{\rho}$, for the same initial data as in Figure 8.

Let us conclude this paper with a comparison of the nonlinear behavior of the perturbations, for which analytical results do not exist, for the cases of a universe dominated by dust and one dominated by a scalar field. In order to start from a situation that is clearly outside the linear regime, we consider initial data such that the value of the energy density at the origin is roughly twice the value of the energy density in the asymptotic homogeneous region. For the case of a universe driven by dust we set the parameters $\bar{\rho}_0 = 2.0 \times 10^{-6}$ and $\delta\rho_* = 2.38 \times 10^{-6}$ in Eq. (38), while for the scalar field we take $\bar{\varphi}_0 = 2 \times 10^{-3}$ and $\varphi_* = 9.611 \times 10^{-4}$ in Eq. (44). In both settings the inhomogeneity has a length-scale of $L = 150$. One should notice that, since we are starting in the nonlinear regime,

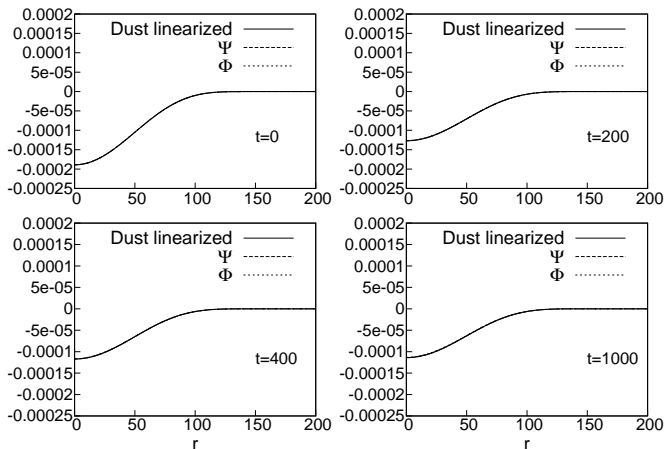


FIG. 10: Similar to Figure 8 but now for an initial data with $L = 150$. We show the results of the numerical evolution of the gauge-invariant quantities $\Psi_{g.i.}$ (dotted-line) and $\Phi_{g.i.}$ (dashed-line), together with the analytic solution obtained in the linear regime for a universe dominated by dust, Eq. (31a) (solid-line).

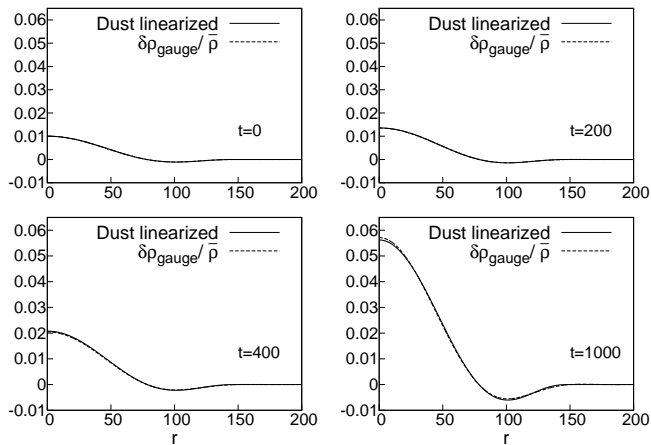


FIG. 11: Similar to Figure 9 but now for an initial data with $L = 150$. We show the results of the numerical evolution of the density contrast (dashed-line), together with the analytic solution obtained in the linear regime for a universe dominated by dust, Eq. (31b) (solid-line).

the construction of the initial data for the scalar field does not result in the same energy density profile as in the case of dust. However, the configurations constructed with these values are in fact very similar and good enough for the comparison (see Figure 12 for details).

The results we show in this case do not correspond directly with the ones observed in the linear regime, since some of the quantities used in that case are now not well defined. This occurs since once we are outside the linear regime the dependence on the choice of slicing becomes relevant. The asymptotic region still evolves as a true background, so long as it is casually disconnected

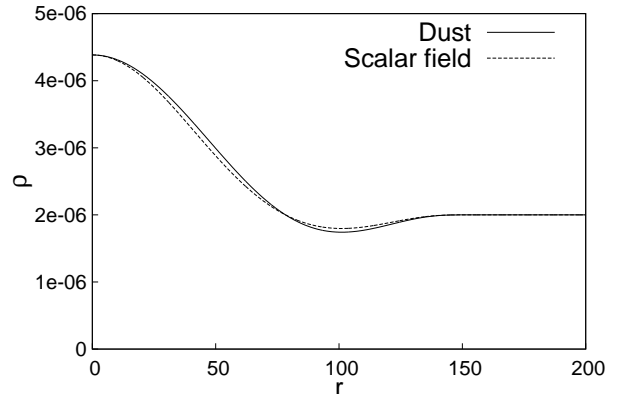


FIG. 12: Initial density profiles used for the evolutions starting in the full nonlinear regime, Figures 13 and 14 below. The parameters were adjusted in order to have initially the same central value of the energy density in dust (solid-line) and in the scalar field (dashed-line).

from the inhomogeneities in the central regions, and then quantities measured by distant observers at rest with respect to this asymptotic background are common to all of them. The question that arises is how we can compare the properties of the spacetime in the central regions to those of the background. It turns out that in spherical symmetry one can consider for this purpose the physical quantities measured by an observer at the origin as functions of proper time, since the spacetime trajectory of this observer is gauge independent for symmetry reasons.

Based on these observations, to study how the inhomogeneity collapses we show in Figure 13 the evolution of the energy density measured by the Eulerian observers as a function of their proper time, evaluated both at the origin and at the boundary of the computational domain. Initially, the energy density at the origin becomes smaller at a similar rate for both the scalar field and dust, as a consequence of the expansion of the universe. However, after some time the central energy density reaches a turnaround point. Both configurations eventually undergo gravitational collapse, forming (small) apparent horizons. Soon thereafter our simulations fail both because our slicing condition is not well adapted to the evolution of black hole spacetimes, and also because our resolution in the central regions is not high enough. In the case of dust the collapse proceeds directly, but for the scalar field once the central density becomes large the effect of the local oscillations dominates so that the collapse to a black hole is delayed.⁸

⁸ Although the details of the collapse to a black hole are not the aim of this paper, it would nevertheless be interesting to study if for the case of a scalar field there is some transient metastable

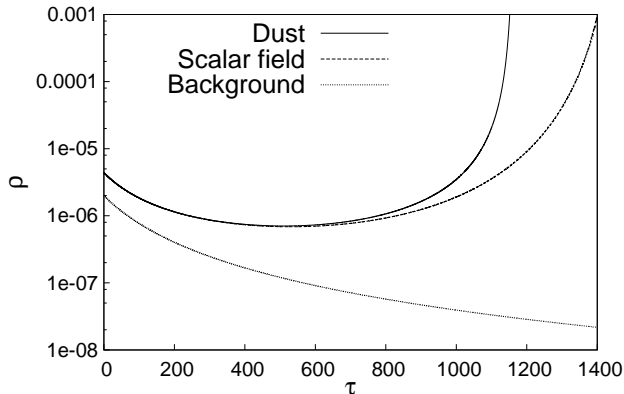


FIG. 13: Evolution of the central energy density measured by the Eulerian observers as a function of proper time τ , for both a universe dominated by dust (solid-line) and one dominated by a scalar field (dashed-line). For comparison we also show the value of the energy density on the boundary of the computational domain (dotted-line). In both cases the central energy density deviates from the asymptotic background evolution, reaching a turnaround point and finally undergoing full gravitational collapse. Meanwhile, the asymptotic region evolves as a true background through the whole simulation.

We also show in Figure 14 the evolution of the trace of the extrinsic curvature at the origin, which encodes the local expansion of the volume elements (one is proportional to the negative of the other). For comparison the value at the boundary is also plotted, all as a function of proper time. Our prescription of initial data assumes that the expansion is initially identical in all the domain, but as soon as the evolution starts the central expansion decreases faster in the over-dense regions. After some transient, however, the effect of our slicing condition causes the expansion at the center to follow closely that of the background. Finally, once the central regions are in a state of full gravitational collapse the expansion deviates again from the background and changes sign. As already discussed above, for the case of dust this leads directly to a black hole, but in the case of the scalar field the effect of the local oscillations become dominant as can be clearly seen in the figure.

VII. CONCLUSIONS

We have used a numerical relativity code in order to follow the evolution of cosmological scenarios with inho-

configuration before a horizon forms. For this one would need to use a better slicing condition that can work well both for the asymptotic background and for the central collapsing regions.

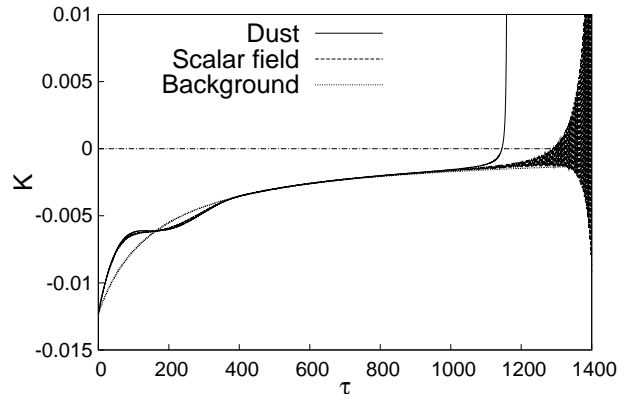


FIG. 14: Central value of the trace of the extrinsic curvature K (essentially the negative of the expansion) as a function of proper time for both dust (solid-line) and scalar field (dashed-line) evolutions. For comparison, the value on the background asymptotic region is also plotted (dotted-line). After a transient when local effects dominate, the value of the expansion catches on with that of the background and deviates again dramatically when reaching a state of full gravitational collapse.

homogeneous, spherically symmetric distributions of matter. When the inhomogeneities are small, both the background energy density and its perturbation decrease as the universe expands, and only the density contrast can grow. In our simulations we have been able to reach and surpass the so-called turn-around point, where the nonlinear terms dominate and the inhomogeneities themselves start to collapse.

We have considered two different situations: a universe dominated by a perfect fluid with no pressure, *i.e.* dust, and one dominated by the coherent oscillations of a massive real scalar field around the minimum of the potential. In both these scenarios matter is described in terms of a field theory and N-body simulations are not viable.

For the case of dust there is a well-known analytic solution that describes the behavior of the homogeneous and isotropic background as well as its small perturbations, and we have shown that our numerical evolutions can reproduce such a solution with high accuracy. For the case of a universe dominated by a scalar field there are no exact analytic expressions. However at late times, when the mass of the scalar particle is much larger than the Hubble parameter, $m \gg H$, our numerical simulations show that the scale factor just oscillates around the solution corresponding to dust, as was already expected from previous approximate studies [5]. These oscillations have small amplitude and high frequency, and damp with the cosmological expansion.

The linear perturbations in the case of the scalar field also evolve in a very similar way as those for dust, as long as their initial size is larger than the Compton wavelength

of the scalar particle, $\lambda_C = 1/m$. On the other hand, initial perturbations in the scalar field with a length-scale of the order of λ_C or shorter do not grow and instead propagate freely with decaying amplitude. This introduces a cutoff in the power spectrum of the scalar field, as has been previously pointed out by other authors in *e.g.* Refs. [31–35]. Once in the nonlinear regime, in the case of dust the initial inhomogeneity simply continues to collapse under its own gravity until a black hole is formed. For the case of the scalar field this final collapse proceeds in a different way: once the central density becomes large the strong local oscillations in the field dominate and the collapse to a black hole is delayed.

The results presented here support the idea that when considering the coherent excitation of a scalar field as a dark matter candidate it is possible to recover similar cosmological large scale structure formation to that obtained with the standard cold dark matter model. Some differences are observed, namely those related to the finite cutoff at short scales, the small high frequency oscillations in the scale factor, and the final state of the gravitational collapse, that may have observational consequences.

Finally we mention some ideas that we leave for future works. First among them there is the problem of forming nonsingular, stable objects starting from inhomogeneous distributions of matter in expanding universes. For the case of dust there is no room for an outcome different to collapse to a black hole. However, if matter is described by the coherent excitation of a scalar field there are well known regular and stable self-gravitating configurations:

oscillatons if the scalar field is real [57, 58], and boson stars for the case of a complex field [59, 60]. It is an open question whether the gravitational collapse of a scalar field in a cosmological context can result in such stable configurations for some choices of the initial data parameters, although this is what one would expect in a successful model of dark matter. On a more practical level, it would be also important to explore different slicing conditions that might allow for longer evolutions in the collapsing regions, as well as to extend our numerical code in order to describe new types of matter (a collection of noncollisional particles described by the Vlasov equation, for example) and more general perturbations in full 3D. In any case, we believe that the study of cosmological nonlinear structure formation within the realm of full general relativity can shed new light on the nature of the mysterious dark components of the universe.

Acknowledgments

We are grateful to Tonatiuh Matos, Olivier Sarbach and Luis Ureña-Lopez for useful comments on a first draft of this paper. This work was partially supported by DGAPA-UNAM under Grants No. IN115311 and No. IN103514, and CONACyT Mexico No. 182445 and No. 167335. JMT acknowledges CONACyT for a graduate grant. ADT is supported in part by Grant No. FQXi-1301 from the Foundational Questions Institute (FQXi).

-
- [1] J. A. Peacock, *Cosmological Physics* (Cambridge University Press, ADDRESS, 1998).
 - [2] S. Dodelson, *Modern Cosmology* (Academic Press, ADDRESS, 2003).
 - [3] V. Mukhanov, *Physical Foundations of Cosmology* (Cambridge University Press, ADDRESS, 2005).
 - [4] M. Kuhlen, M. Vogelsberger, and R. Angulo, *Physics of the Dark Universe* **1**, 50 (2012).
 - [5] M. Dine and W. Fischler, *Phys.Lett.* **B120**, 137 (1983).
 - [6] J.-w. Lee and I.-g. Koh, *Phys.Rev.* **D53**, 2236 (1996).
 - [7] W. Hu, R. Barkana, and A. Gruzinov, *Phys.Rev.Lett.* **85**, 1158 (2000).
 - [8] P. Sikivie and Q. Yang, *Phys.Rev.Lett.* **103**, 111301 (2009).
 - [9] A. Suarez, V. Robles, and T. Matos, arXiv:1302.0903 (2013).
 - [10] P. Peebles and B. Ratra, *Rev.Mod.Phys.* **75**, 559 (2003).
 - [11] S. Tsujikawa, *Class.Quant.Grav.* **30**, 214003 (2013).
 - [12] C. Armendariz-Picon, V. F. Mukhanov, and P. J. Steinhardt, *Phys.Rev.* **D63**, 103510 (2001).
 - [13] M. Milgrom, *Acta Phys.Polon.* **B32**, 3613 (2001).
 - [14] J. D. Bekenstein, *Phys.Rev.* **D70**, 083509 (2004).
 - [15] C. Eling, T. Jacobson, and D. Mattingly, 163 (2004).
 - [16] T. Jacobson, arXiv:0801.1547 (2008).
 - [17] K. Hinterbichler, *Rev.Mod.Phys.* **84**, 671 (2012).
 - [18] C. de Rham, *Living Rev.Rel.* **17**, 7 (2014).
 - [19] M. Alcubierre and M. D. Mendez, *Gen.Rel.Grav.* **43**, 2769 (2011).
 - [20] M. Alcubierre, *Introduction to 3+1 Numerical Relativity* (Oxford Univ. Press, New York, 2008).
 - [21] M. Ruiz, M. Alcubierre, and D. Nunez, *Gen.Rel.Grav.* **40**, 159 (2008).
 - [22] M. Alcubierre *et al.*, *Phys.Rev.* **D81**, 124018 (2010).
 - [23] M. Ruiz *et al.*, *Phys.Rev.* **D86**, 104044 (2012).
 - [24] J. M. Torres and M. Alcubierre, *Gen.Rel.Grav.* **46**, 1773 (2014).
 - [25] J. Garriga and V. F. Mukhanov, *Phys.Lett.* **B458**, 219 (1999).
 - [26] R. J. Scherrer, *Phys.Rev.Lett.* **93**, 011301 (2004).
 - [27] M. Alcubierre, A. de la Macorra, A. Diez-Tejedor, and J. M. Torres, (In preparation).
 - [28] M. Shibata and T. Nakamura, *Phys.Rev.* **D52**, 5428 (1995).
 - [29] T. W. Baumgarte and S. L. Shapiro, *Phys.Rev.* **D59**, 024007 (1998).
 - [30] J. D. Brown, *Phys.Rev.* **D79**, 104029 (2009).
 - [31] B. Ratra, *Phys.Rev.* **D38**, 2399 (1988).
 - [32] J.-c. Hwang, *Phys.Lett.* **B401**, 241 (1997).
 - [33] T. Matos and L. A. Urena-Lopez, *Class. Quant. Grav.* **17**, L75 (2000).
 - [34] T. Matos and L. A. Urena-Lopez, *Phys.Rev.* **D63**, 063506 (2001).

- [35] D. J. Marsh and P. G. Ferreira, *Phys.Rev.* **D82**, 103528 (2010).
- [36] H.-Y. Schive, T. Chiueh, and T. Broadhurst, *Nature Physics* **10**, 496 (2014).
- [37] H.-Y. Schive *et al.*, arXiv:1407.7762 (2014).
- [38] J. Adamek, D. Daverio, R. Durrer, and M. Kunz, *Phys.Rev.* **D88**, 103527 (2013).
- [39] M. Bruni, D. B. Thomas, and D. Wands, *Phys.Rev.* **D89**, 044010 (2014).
- [40] M. Bruni, J. C. Hidalgo, and D. Wands, arXiv:1405.7006 (2014).
- [41] G. Rigopoulos, arXiv:1409.6549 (2014).
- [42] L. A. Urena-Lopez, *Phys.Rev.* **D90**, 027306 (2014).
- [43] J. Reker, I. Cordero-Carrion, and A. Fuzfa, arXiv:1409.3476 (2014).
- [44] C. L. Wainwright *et al.*, *JCAP* **1403**, 030 (2014).
- [45] C. L. Wainwright, M. C. Johnson, A. Aguirre, and H. V. Peiris, *JCAP* **1410**, 024 (2014).
- [46] R. Arnowitt, S. Deser, and C. W. Misner, in *Gravitation: An Introduction to Current Research*, edited by L. Witten (John Wiley, New York, 1962), pp. 227–265.
- [47] J. York, in *Sources of Gravitational Radiation*, edited by L. Smarr (Cambridge University Press, Cambridge, England, 1979).
- [48] J. A. Font, J. M. Ibanez, A. Marquina, and J. M. Marti, *Astron.Astrophys.* **282**, 304 (1994).
- [49] B. Gustafsson, H. Kreiss, and J. Olinger, *Time dependent problems and difference methods* (Wiley, New York, 1995).
- [50] D. N. Vulcanov and M. Alcubierre, *Int.J.Mod.Phys.* **C13**, 805 (2002).
- [51] C. Bona, J. Massó, E. Seidel, and J. Stela, *Phys.Rev.Lett.* **75**, 600 (1995).
- [52] J. M. Bardeen, *Phys.Rev.* **D22**, 1882 (1980).
- [53] J. A. Font, *Living Rev.Rel.* **11**, 7 (2008).
- [54] R. J. Leveque, *Numerical Methods for Conservation Laws* (Birkhauser Verlag, Basel, 1992).
- [55] D. H. Lyth and A. R. Liddle, *The primordial density perturbation: Cosmology, inflation and the origin of structure* (Cambridge University Press, ADDRESS, 2009).
- [56] M. S. Turner, *Phys. Rev.* **D28**, 1243 (1983).
- [57] E. Seidel and W. Suen, *Phys.Rev.Lett.* **66**, 1659 (1991).
- [58] M. Alcubierre *et al.*, *Class. Quant. Grav.* **20**, 2883 (2003).
- [59] R. Ruffini and S. Bonazzola, *Phys.Rev.* **187**, 1767 (1969).
- [60] S. L. Liebling and C. Palenzuela, *Living Rev.Rel.* **15**, 6 (2012).